CHEMISTRY OF MATERIALS

Article

pubs.acs.org/cm

Cu_2ZnSnS_4 Thin Films Generated from a Single Solution Based Precursor: The Effect of Na and Sb Doping

Devendra Tiwari,[†] Tristan Koehler,[§] Xianzhong Lin,[§] Robert Harniman,[†] Ian Griffiths,[‡] Lan Wang,[§] David Cherns,[‡] Reiner Klenk,[§] and David J. Fermin*[,†]

[†]School of Chemistry, University of Bristol, Cantock's Close, Bristol BS8 1TS, United Kingdom

[‡]H.H. Wills Physics Laboratory, University of Bristol, Tyndall Av., Bristol BS8 1TL, United Kingdom

[§]Helmholtz-Zentrum Berlin für Materialien und Energie, Hahn-Meitner-Platz 1, D-14109 Berlin, Germany

Supporting Information

ABSTRACT: A new solution based route for depositing Cu_2ZnSnS_4 (CZTS) thin films is described, focusing on the effects of Sb and Na codoping. X-ray diffraction and Raman spectroscopy confirm formation of the kesterite phase with a measurable improvement in crystallinity upon doping. A sharp band gap absorption edge at 1.4 eV is determined from diffuse reflectance measurements, while improvement in the photoluminescence yield and sharpening of the band-to-band emission spectra are observed in the presence of Na and Sb. The performance of devices with the configuration glass/Mo/CZTS/CdS/i-ZnO/ZnO:Al/Ni−Al and total area of 0.5 cm^2 is reported. Analysis of over 200 cells shows that introduction of Na and Sb leads to an increase of the average power conversion efficiency from 3.2 ± 0.6 to 5.2 ± 0.3%. The best cell with efficiency of 5.7% is obtained upon Na and Sb doping, featuring 14.9 mA cm^{-2} short-circuit current, 610 mV open circuit voltage, and 63% fill factor under simulated AM 1.5 illumination. This performance ranks among the highest in pure sulfide CZTS cells. We propose that the improvement in crystallinity and cell performance is linked to the formation of alkali antimony chalcogenides flux during the annealing step, in addition to Sb and Na decreasing disorder in specific lattice positions of the CZTS unit cell.

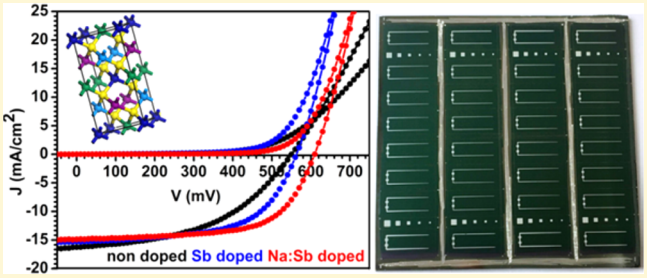

1. INTRODUCTION

$Cu_2ZnSn(S,Se)_4$ based materials are widely considered as a potential alternative to $Cu(In,Ga)(S,Se)_2$ absorbers (CIGS) in thin-film photovoltaic (PV) technology. Research in this area is driven by the developing scalable PV technologies featuring earth-abundant elements and low-cost processing.[1] State-of-art of $Cu_2ZnSn(S,Se)_4$ lab scale cells have delivered power conversion efficiency of 12.6% in the so-called substrate configuration featuring antireflection coating (ARC).[2] These high performing thin films were generated by solution processing, containing hydrazine precursors and binary chalcogenides.[2] Devices containing Cu_2ZnSnS_4 (CZTS) and $Cu_2ZnSn(S,Se)_4$ (CZTSSe) obtained by metal sputtering and reactive annealing have reached record efficiencies of 9.2% (with ARC) and 11.8% (with ARC), respectively.[3,4] Recently there has been an increasing interest in nonhydrazine based solution routes which can directly scale to roll-to-roll processing.[5] In this direction, a variety of solution based approaches have been described in recent years including nanocrystalline colloidal precursors, dimethyl-sulfoxide based molecular precursor, and electrodeposition.[6−8] The highest performances obtained for CZTS and CZTSSe via direct liquid processing (without antireflecting coating) are 5.5 and 11.8%, respectively.[7,9] Despite important efforts in developing preparation methods for high quality CZTSSe films, devices consistently show lower efficiencies than state-of-the-art CIGS systems, in particular low open circuit voltages (V_{OC}).

The performance of solution based layers could be affected by (i) incomplete conversion of molecular precursors leading to poorly crystalline domain as well as (ii) the presence of secondary phases and point defects emerging at temperatures close to the CZTSSe phase formation.[10−14] Both types of defects can be detrimental to key device metrics such as short-circuit current density (J_{SC}), fill factor (ff), and V_{OC}. The most efficient devices have been reported for Cu-poor and Zn-rich films, which have been linked to a decrease in cation disorder upon phase formation.[15] The inclusion of dopants such as Li, Na, K, Cs, Sb, and Bi has also been investigated in order to facilitate phase formation and to improve the film microstructure.[7,16−19] Na doping has led to significant improvement in CIGS devices and, to a certain extent, CZTSSe cells.[20,21] The role of Na has been connected to an increase in the effective doping level, leading to higher open circuit voltage when dominant recombination lies in the space charge region. Furthermore, increasing doping carrier density improves electrical contact with the $Mo(S/Se)_2$ support. Although the

Received: April 14, 2016
Revised: June 20, 2016
Published: June 20, 2016

DOI: 10.1021/acs.chemmater.6b01499
Chem. Mater. 2016, 28, 4991−4997

effect of other dopants is commonly associated with improvement in grain growth and defect passivation, their precise action mechanism is yet to be fully elucidated.

The present report describes a new methodology for preparing high quality CZTS films based on dimethyl-formamide solution containing the metal cations and thiourea, as well as Na and Sb dopants. Films with thickness of about 1.2 μm are deposited by a sequential spin-coating heating procedure on Mo coated glass, followed by annealing at 560 °C. Infrared spectroscopy and differential scanning calorimetry (DSC) is employed to investigate the early stages in the CZTS phase formation. X-ray diffraction (XRD) and atomic force microscopy in conjunction with Raman, photoluminescence, and diffuse reflectance spectroscopy reveal the formation of compact and crystalline CZTS films, featuring a 1.4 eV band gap and a high degree of phase purity. Devices fabricated in the substrate configuration clearly show an improved performance upon addition of Na and Sb to the precursor solution. Na:Sb codoped films yield efficiencies up to 5.7%, with V_{OC}, *ff*, and J_{SC} values of 610 mV, 63%, and 14.9 mA cm^{-2}, respectively. This performance recorded in 0.5 cm^2 cells without ARC is among the highest reported for CZTS films.[3,8,9,13,14,22]

2. RESULTS AND DISCUSSION

Thin films are prepared by sequential spin-coating steps of (1:1) dimethyl-formamide and 2-propanol solutions containing chloride salts Cu(II), Zn(II), and Sn(II) in a ratio of 1.8:1.5:1.0, respectively. Thiourea is used as sulfur precursor. The Sb and Na dopants are added directly into the precursor solution in the form of $Sb(OAc)_3$ and NaCl (Sb/Na = 5). Film deposition involves four spin-coating steps at 2000 rpm, with heating steps at 300 °C in air for 2 min between each addition. After deposition, the films are annealed in a N_2/H_2 mixture in the presence of S at 560 °C for 30 min. Further details in the preparation of the film are described in the Experimental Section.

Figure 1a contrasts the IR spectra of thiourea and precursor films obtained after drying in vacuum at room temperature. The spectra show a 40 cm^{-1} red shift of the C═S stretching mode in the precursor films in comparison to thiourea. A blue shift (10−15 cm^{-1}) can also be seen in the coupled C—N stretching and N—H bending modes as well as in the N—H stretching mode. These changes in the vibrational modes indicate a decrease in C═S bond order along with an increase in the C—N bond order, suggesting a charge transfer complexation of thiourea to metal ion via S site (depicted schematically as inset in Figure 1a). Several subtle shifts in the thiourea vibrational modes originating from changes in symmetry and increase in bond stiffness can be identified as shown in Table S1 (Supporting Information).[23] Similar IR responses are observed for the precursor in the presence of Sb and Na.

TGA and DSC curves for the dry precursor in the presence and absence of the dopants are shown in Figure 1b. TGA data display a sharp weight loss step between 170 and 270 °C. DSC indicates that this process is exothermic and can be attributed to the formation of sulfides from the metal−thiourea complex. DSC also shows a very prominent endothermic peak at 480 °C, with no weight loss, which is linked to the formation of the CZTS phase. The minimum of the DSC curve decreases upon addition of Sb and Na:Sb as illustrated in the inset of Figure 1b. This key observation provides very strong evidence that the dopant facilitates the crystallization of the CZTS phase. We

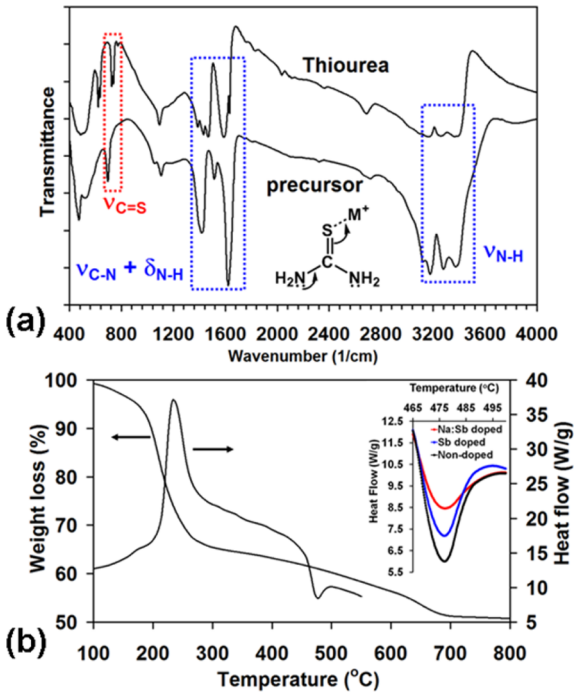

Figure 1. IR spectra of dry thiourea and precursor films, highlighting changes in key vibrational modes associated with metal−sulfur interactions as depicted in the inset (a). Thermogravimetric and differential scanning calorimetry of the precursor solution (b). Inset shows the effect of doping on the DSC peak.

suggest that this effect is linked to the formation of Sb_2S_3 and $NaSb_5S_8$ (Na and Sb are added in 1:5 ratio) under S rich annealing conditions. The crystallization temperature of Sb_2S_3 is 320 °C, while $NaSb_5S_8$ is expected to undergo a glass to crystal phase transition around 287 °C.[24,25]

Figure 2 contrasts the XRD patterns and Raman spectra of the annealed CZTS films in the presence and absence of the dopants. The XRD patterns are characterized by sharp and intense peaks in comparison to the rather broad and featureless patterns observed for nonannealed films (see Figure S1 of the Supporting Information). Qualitatively, an increase in the intensity of the XRD peaks in the presence of the dopants can also be seen (Figure 2a). All of the XRD peaks (except the one associated with the Mo substrate) match the standard JCPDS file for the CZTS kesterite phase. The formation of the kesterite phase is further confirmed by the Raman spectra shown in Figure 2b. The spectra for doped and nondoped films exhibit signature peaks associated with the A-mode at 288 and 336, as well as the B/E symmetry mode at 365 cm^{-1} of CZTS.[14] An improvement in the intensity and peak width upon doping of the film, in particular for the Na:Sb codoping, can also be seen.

The results of the Rietveld analysis of the XRD patterns are graphically shown in Figure 2a, while the structural parameters including site locations, occupancies, isotropic temperature factors (B_{iso}), and lattice parameters are included in the Supporting Information (Table S2).[26] Excellent fits were obtained to the $I\bar{4}$ space group of tetragonal lattice, with quality coefficients R_p and R_{wp} ranging between 3.98 to 4.27% and 6.2 to 7.05%, respectively. The analysis also allowed estimating the presence of secondary phases, yielding less than 15% of the ZnS sphalerite phase. The stoichiometry, as calculated from the site occupancies, is consistent with a Cu-

DOI: 10.1021/acs.chemmater.6b01499
Chem. Mater. 2016, 28, 4991−4997

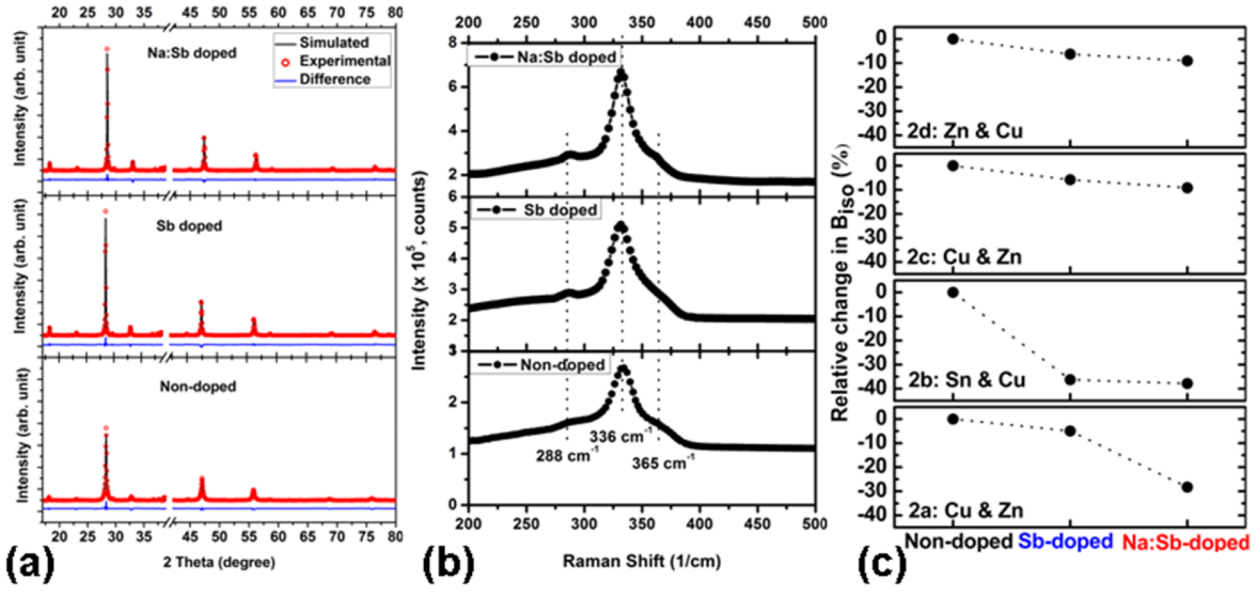

Figure 2. X-ray diffractograms (a) and Raman spectra (b) for annealed CZTS films in the absence of dopants and for Sb and Na:Sb doped films. Relative change (with respect to nondoped) in isotropic temperature factors (B_{iso}) at metal sites obtained by Rietveld refinement of the XRD patterns. (c) Full analysis of the refinements are provided in the Supporting Information (Table S2).

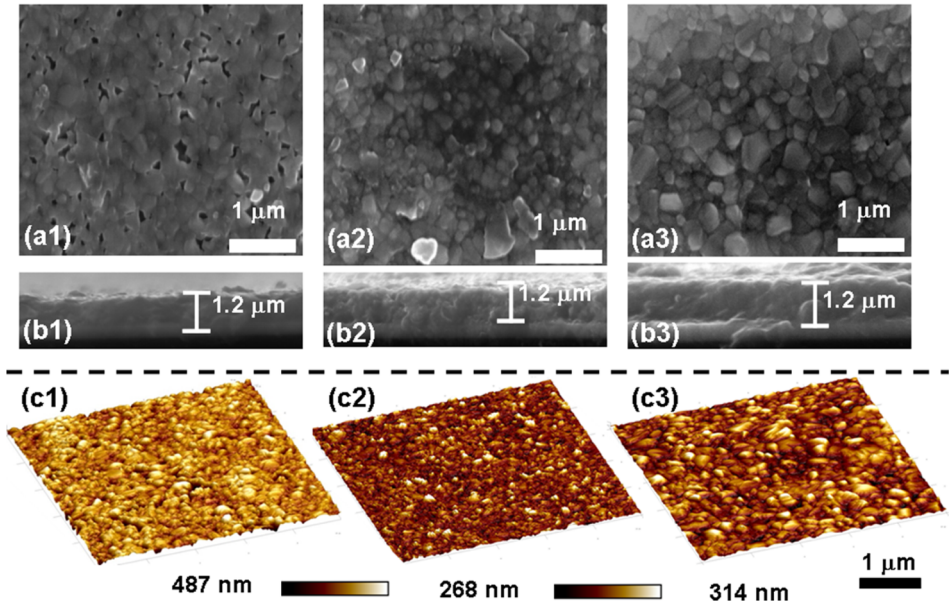

Figure 3. Top (a) and cross-sectional (b) scanning electron micrographs as well as (c) 3-D atomic force microscopy images of the CZTS films. Images correspond to nondoped (1), Sb doped (2), and (3) Na:Sb codoped annealed films on Mo coated glass substrates.

poor and Zn-rich composition. Energy dispersive X-rays analysis (Table S3) showed composition ratios ([Zn] + [Sn])/[Cu] of 1.3 and [Zn]/[Sn] of 1.4, which is very close to the composition of the molecular precursor. This stoichiometry has been described as optimum for efficient CZTS devices.[14]

In order to facilitate discussions on dopant effects, a schematic representation of the kesterite of the unit cell is depicted in Figure S2 with color coding of the lattice sites. The lattice parameters only show a slight increase in the presence of Na, suggesting a degree of isovalent substitution of Cu atoms. Cation site occupancies also appear little affected by the presence of dopants. The most important observation in this analysis is the variation of the B_{iso} sites upon doping as shown in Figure 2c. The introduction of Sb leads to a decrease in B_{iso} associated with the 2b site, which is essentially dominated by the Sn atoms. Similarly, the introduction of Na decreases B_{iso} at the copper occupied 2a site. This behavior can be rationalized considering that Sb has a similar ionic radius as Sn, while Na is isovalent with Cu. Temperature factors are linked to the scattering efficiency of a basis, providing a good indication of the level of structural disorder.[27] Consequently, we can conclude that the increase in the degree of crystallization is linked to preferential interactions of Sb with Sn and Na with Cu ions, leading to a decrease in site disorder. This view is significantly different from current discussions in the literature proposing that alkali metals affect electric fields in grain boundaries.[7]

DOI: 10.1021/acs.chemmater.6b01499
Chem. Mater. 2016, 28, 4991−4997

The morphology of the CZTS films as probed by SEM and AFM are shown in Figure 3, contrasting the effect of Sb and Na:Sb codoping. The SEM images (Figure 3a) show a clear increase in the grain sizes upon Sb and Na:Sb doping with respect to the nondoped films, with the latter showing some gaps at the surface. The cross section SEM images (Figure 3b) further illustrate the increase in grain size upon doping, while all the films appear compact with a mean thickness of 1.2 μm. The AFM images (Figure 3c) reveal a slight increase in the mean roughness from 33 to 63 nm (in micrometer range) upon doping of the films. This trend is also consistent with the DSC and XRD analysis, confirming that doping leads to larger degree of crystallinity in the annealed films.

Figure 4 compares the diffuse reflectance and room temperature photoluminescence (PL) spectra (514 nm excitation) of nondoped and doped CZTS films. The reflectance shows sharp onset around 835 nm associated with the band-to-band transition, as well as interference patterns confirming the highly homogeneous and compact nature of the films. The intensity of the interference patterns appears to dampen upon Sb doping and Na:Sb codoping, which is probably linked to the increase in film roughness revealed by AFM (Figure 3). Tauc representation of the reflectance data, expressed in terms of the Kubelka–Munk function, allows estimating an optical band gap of 1.4 eV for CZTS films regardless the presence of dopants (see Supporting Information Figure S3). On the other hand, the PL spectra are characterized by a broad band which tends to narrow and shift the maximum toward 1.4 eV with Na:Sb codoping. To a first approximation, these responses can be deconvoluted into two Voigt peaks, although more complex analyses have been described in other works.[28] One of the peaks is fixed at 1.39 eV, which is assigned to band-to-band (BB) recombination. The position of the second peak is allowed to be adjusted, showing a systematic increase in the peak position (up to 0.08 eV) and decrease in intensity upon Na:Sb codoping. Interestingly, Grossberg et al. have rationalized the presence of this additional PL signal in terms of Sn based defects.[28] The fact that defect related PL features are damped upon codoping provides good indication that the presence of Na:Sb can have a significant impact on cell performance.

The performance of PV devices with the structure SLG/Mo/CZTS/CdS/i-ZnO/ZnO:Al/Ni–Al (0.5 cm^2, without antireflective coating) is shown in Figure 5. J–V characteristics under simulated AM1.5G illumination (Figure 5a) and external quantum efficiency (EQE, Figure 5b) spectra of the best cells clearly show an improvement in performance upon doping with Sb and Na:Sb. All samples show EQE values above 75%, although the red response slightly improves upon doping. The inset to Figure 5b shows an image of a typical array of cells fabricated on a 5 × 5 cm^2 substrate. Figure 5c shows a cross-section (generated by focused ion beam) SEM image of a device featuring a nondoped CZTS film. The elemental distribution across the same device is shown in Figure S4. One of the key features in this image is the presence of voids in the absorber layer. This is consistent with the topographic features shown in Figure 3. More detailed microscopic studies of device structure as a function of doping will be reported elsewhere.

The evolution of the mean cell efficiency (η), ff, J_{SC}, and V_{OC} for 72 cells of each composition is summarized in Figure 6. The statistical analysis further supports a clear increase in cell efficiency upon doping, as well as in fill factor. With regards to

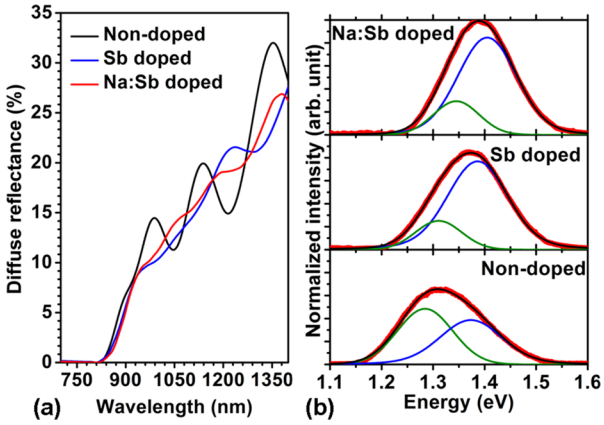

Figure 4. Diffuse reflectance spectra (a) and room temperature photoluminescence spectra (b) of annealed films with the different dopants.

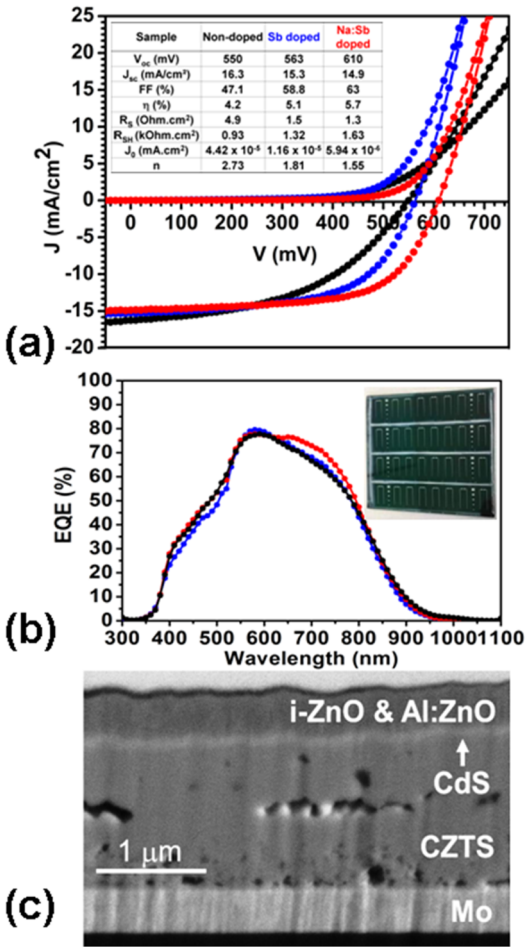

Figure 5. J–V curves under simulated AM1.5G (a) and external quantum efficiency (EQE) spectra of the best cells with inset showing cross-section SEM image of a device fabricated out of nondoped CZTS and a picture of a typical array of devices on 5 × 5 cm^2 substrates (b). Cross-section scanning electron micrograph of a device completed out of a nondoped CZTS film (c). Devices were front illuminated with architecture SLG/Mo/CZTS/CdS/i-ZnO/ZnO:Al/Ni–Al, featuring a total area of 0.5 cm^2 measured at 23 °C.

DOI: 10.1021/acs.chemmater.6b01499
Chem. Mater. 2016, 28, 4991–4997

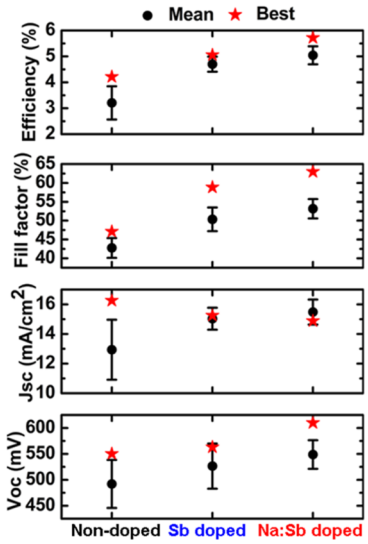

Figure 6. Variation in solar cell parameters: open-circuit voltage (V_{OC}), short-circuit current density (J_{SC}), fill factor, and efficiency, for 72 devices fabricated from each type of CZTS film: nondoped, Sb-doped, and Na:Sb doped. Red stars and black dots indicate best and mean values for a parameter, respectively. Devices were front illuminated with architecture SLG/Mo/CZTS/CdS/i-ZnO/ZnO:Al/Ni–Al, featuring a total area of 0.5 cm^2 measured at 23 °C.

V_{OC} and J_{sc}, there is a significant variation in nondoped samples which decreases along with an increase in the mean values upon doping.

The ensemble of the data displays a significant effect arising from Na:Sb doping, including the following:

1. Disappearance (or shift to higher voltages) of the crossover in the $J-V$ curves in the dark and under illumination and decrease in series resistance with no significant shunt indicate alleviation of voltage dependent photocurrent collection.
2. Decrease in reverse saturation current (J_O) and diode ideality factor (n) suggests a shift dominant recombination pathway from interface to bulk.

These observations are consistent with an improvement in crystallinity, more compact films, and an increase in effective carrier density, as well as reduction of interfacial and intrinsic defects upon doping.[29] However, conclusive insight into the transport mechanism would require temperature and light intensity dependence measurements, which will be studied separately. The best cell was obtained with Na:Sb codoped films with η = 5.7%, J_{SC} = 14.9 mA cm^{-2}, V_{OC} = 610 mV, and ff = 63%. Average fill factors are still below the best reported values which is most probably associated with a large degree of sulfurization of the Mo substrate upon annealing. There is also a significant effect of the CdS layer in the EQE responses below 550 nm which can be alleviated by optimizing the film thickness. Additional dopants may also decrease band tails associated with sub-band gap states. Recently, Ag alloying in CZTS lattice has been found to significantly suppress these tail states.[30] In any case, this report clearly demonstrates that our single solution precursor methodology can provide high quality CZTS films, while the introduction of dopants such as Na and Sb plays a clear role in facilitating crystal growth and minimizing structural disorder.

3. CONCLUSIONS

A new formulation for generating high-quality CZTS thin films based on the deposition of a single precursor solution is described, focusing on the role of Sb and Na:Sb doping. The precursor solution contains chloride salts of the metals and thiourea dissolved in a mixture of dimethyl-formamide and isopropanol. For the first time, we demonstrate that the introduction of Na and Sb lowers the energetic requirement of crystallization with improved crystallization and reduced disorder by interacting with Cu and Sn sites, respectively, as determined by DSC and quantitative XRD analysis. The fact that Na:Sb codoping provides substantial improvement in performance, in comparison to only Na or Sb, points toward the formation of an alkali antimony chalcogenides flux during the annealing step. These interactions manifest themselves in better defined Raman and photoluminescence responses. Devices with the configuration SLG/Mo/CZTS/CdS/i-ZnO/ZnO:Al/Ni–Al show statistically relevant improvement in cell efficiency upon Na:Sb doping, with the best cell showing a power conversion efficiency of 5.7%. In general, devices show decent V_{oc} and ff, and J_{SC} of the device can be improved with additional antireflective on the device. We believe this approach has tremendous potential for generating high performing thin-film devices given the flexibility and scalability of single solution based precursors.

4. EXPERIMENTAL SECTION

CZTS films are deposited onto 500 nm thick Molybdenum coated 5 × 5 cm^2 glass substrates (M-Solv, U.K.) by spin coating a precursor solution and heating it to convert it into solid CZTS films. The precursor solution consists of a dimethyl-formamide (DMF) and 2-propanol mix (1:1) as solvent (formamide instead of DMF can also be employed), with chlorides of Cu(II), Zn(II), and Sn(II) dissolved in 1.8:1.5:1 proportion as metal source and thiourea as S source. 1% $Sb(OAc)_3$ and 0.2% of NaCl is added to CZTS precursor solution as dopants sources (Sb/Na = 5). All the reagents were purchased from Sigma-Aldrich. A total 100 μL of precursor solution is dropped on the substrates and spun-coated at 2000 rpm for 1 min, followed by heating on a hot plate at 300 °C for 2 min in air. This process is repeated four times to obtain a film thickness of nearly 1200 nm. Films are placed in a graphite box with S powder and annealed in a rapid thermal annealing furnace (MTI-OTF1200X) at 560 °C for 30 min. These films do not contain a blocking layer between soda-lime glass substrate and the molybdenum layer, typically used to prevent Na diffusion to absorber layer. Additional Na doping (without Sb) led to device performances similar to those obtained for nondoped samples. The results for cells fabricated out of solely Na doping are summarized in Figure S5. Films are etched in 10% aqueous KCN solution for 30 s, followed by chemical bath deposition of the CdS buffer layer, from an aqueous bath containing $CdSO_4$, thiourea, and ammonium hydroxide, at 70 °C. Deposition of i-ZnO and aluminum doped ZnO window layer were performed by sputtering. Finally, a Ni/Al contact grid on top of the solar cell was deposited by evaporation using a shadow mask. Solar cells with a total area of 0.5 cm^2 were defined by mechanical scribing. No antireflection coating is employed. $J-V$ characteristics of the completed device are measured in dark and under illumination using an in-house class A solar simulator with simulated AM 1.5 G spectrum and integrated power density of 100 mW/cm^2 at 23 °C. External quantum efficiency of the cells is attained using dual illumination from halogen and xenon lamps and a Bentham TM 300 monochromator (Bentham instruments). Calibrated Si and Ge photodiodes are used as references for illumination source in $J-V$ characteristics and quantum efficiency measurements.

DOI: 10.1021/acs.chemmater.6b01499
Chem. Mater. 2016, 28, 4991–4997

■ ASSOCIATED CONTENT

Supporting Information

The Supporting Information is available free of charge on the ACS Publications website at DOI: 10.1021/acs.chemmater.6b01499.

Film characterization details, table assigning the vibrational modes in Infrared spectra, schematic of crystal structure with labeled atomic sites, tables detailing various structural parameters estimated from Rietveld refinement, table listing atomic composition as determined from EDS, and modified Tauc plot from diffuse reflectance for estimating band gap (PDF)

■ AUTHOR INFORMATION

Notes

The authors declare no competing financial interest.

■ ACKNOWLEDGMENTS

D.T. and D.J.F. are grateful to the funding by the UK Engineering and Physical Sciences Research Council (EPSRC) via the PVTEAM Programme (EP/L017792/1). D.J.F. acknowledges the support by the Institute of Advanced Studies of the University of Bristol (University Research Fellowship 2015). Microscopy analysis was performed at the Chemical Imaging Facility, University of Bristol, with equipment funded by EPSRC Grant "Atoms to Applications" (EP/K035746/1). The authors are also indebted by the support from the Helmholtz Zentrum für Materialien und Energie Berlin.

■ REFERENCES

(1) Repins, I.; Vora, N.; Beall, C.; Wei, S.-H.; Yan, Y.; Romero, M.; Teeter, G.; Du, H.; To, B.; Young, M.; Noufi, R. Kesterites and Chalcopyrites: A Comparison of Close Cousins. *MRS Online Proc. Libr.* **2011**, *1324*, d17.

(2) Wang, W.; Winkler, M. T.; Gunawan, O.; Gokmen, T.; Todorov, T. K.; Zhu, Y.; Mitzi, D. B. Device Characteristics of CZTSSe Thin-Film Solar Cells with 12.6% Efficiency. *Adv. Energy Mater.* **2014**, *4*, 1301465.

(3) Hiroi, H.; Sakai, N.; Kato, T.; Sugimoto, H. High Voltage Cu_2ZnSnS_4 Submodules by Hybrid Buffer Layer. *2013 IEEE 39th Photovolt. Spec. Conf.* **2013**, 0863−0866.

(4) Hiroi, H.; Sakai, N.; Iwata, Y.; Kato, T.; Sugimoto, H. Impact of Buffer Layer on Kesterite Solar Cells. *2015 IEEE 42nd Photovolt. Spec. Conf.* **2015**, 1−4.

(5) Todorov, T.; Mitzi, D. B. Direct Liquid Coating of Chalcopyrite Light-Absorbing Layers for Photovoltaic Devices. *Eur. J. Inorg. Chem.* **2010**, *2010*, 17−28.

(6) Miskin, C. K.; Yang, W.; Hages, C. J.; Carter, N. J.; Joglekar, C. S.; Stach, E. A.; Agrawal, R. 9.0% Efficient $Cu_2ZnSn(S,Se)_4$ Solar Cells from Selenized Nanoparticle Inks. *Prog. Photovoltaics* **2015**, *23*, 654−659.

(7) Xin, H.; Vorpahl, S. M.; Collord, D.; Braly, I. L.; Uhl, R.; Krueger, B. W.; Ginger, D. S.; Hillhouse, H. W. Lithium-Doping Inverts the Nanoscale Electric Field at the Grain Boundaries in $Cu_2ZnSn(S,Se)_4$ and Increases Photovoltaic Efficiency. *Phys. Chem. Chem. Phys.* **2015**, *17*, 23859−23866.

(8) Jiang, J. S.; Ikeda, S.; Harada, T.; Matsumura, M. Pure Sulfide Cu_2ZnSnS_4 Thin Film Solar Cells Fabricated by Preheating an Electrodeposited Metallic Stack. *Adv. Energy Mater.* **2014**, *4*, 1301381.

(9) Zhou, F.; Zeng, F.; Liu, X.; Liu, F.; Song, N.; Yan, C.; Pu, A.; Park, J.; Sun, K.; Hao, X. Improvement of J_{sc} in a Cu_2ZnSnS_4 Solar Cell by Using a Thin Carbon Intermediate Layer at the Cu_2ZnSnS_4/Mo Interface. *ACS Appl. Mater. Interfaces* **2015**, *7*, 22868−22873.

(10) Carrete, A.; Shavel, A.; Fontané, X.; Montserrat, J.; Fan, J.; Ibáñez, M.; Saucedo, E.; Pérez-Rodríguez, A.; Cabot, A. Antimony-Based Ligand Exchange to Promote Crystallization in Spray-Deposited $Cu_2ZnSnSe_4$ Solar Cells. *J. Am. Chem. Soc.* **2013**, *135*, 15982−15985.

(11) Siebentritt, S. Why Are Kesterite Solar Cells Not 20% Efficient? *Thin Solid Films* **2013**, *535*, 1−4.

(12) Chen, S.; Walsh, A.; Gong, X.-G.; Wei, S.-H. Classification of Lattice Defects in the Kesterite Cu_2ZnSnS_4 and $Cu_2ZnSnSe_4$ Earth-Abundant Solar Cell Absorbers. *Adv. Mater.* **2013**, *25*, 1522−1539.

(13) Kumar, M.; Dubey, A.; Adhikari, N.; Venkatesan, S.; Qiao, Q. Strategic Review of Secondary Phases, Defects and Defect-Complexes in Kesterite CZTS−Se Solar Cells. *Energy Environ. Sci.* **2015**, *8*, 3134−3159.

(14) Huang, T. J.; Yin, X.; Qi, G.; Gong, H. CZTS-Based Materials and Interfaces and Their Effects on the Performance of Thin Film Solar Cells. *Phys. Status Solidi RRL* **2014**, *08*, 735−762.

(15) Paris, M.; Choubrac, L.; Lafond, A.; Guillot-Deudon, C.; Jobic, S. Solid-State NMR and Raman Spectroscopy To Address the Local Structure of Defects and the Tricky Issue of the Cu/Zn Disorder in Cu-Poor, Zn-Rich CZTS Materials. *Inorg. Chem.* **2014**, *53*, 8646−8653.

(16) Bodegard, M.; Stolt, L.; Hedstrom, J. Presented at 12th European Photovoltaic Solar Energy Conference (EU PVSEC 12), Amsterdam, Netherlands, April 11−15, 1994.

(17) Contreras, M. A.; Egaas, B.; Dippo, P.; Webb, J.; Granata, J.; Ramanathan, K.; Asher, S.; Swartzlander, A.; Noufi, R. On the Role of Na and Modifications to $Cu(In,Ga)Se_2$ Absorber Materials Using Thin-MF (M = Na, K, Cs) Precursor Layers. *1997 IEEE 26th Photovolt. Spec. Conf.* **1997**, 359−362.

(18) Nakakoba, H.; Yatsushiro, Y.; Mise, T.; Kobayashi, T.; Nakada, T. Effects of Bi Incorporation on $Cu(In_{1-x}Ga_x)Se_2$ Thin Films and Solar Cells. *Jpn. J. Appl. Phys.* **2012**, *51*, 10S.

(19) Yuan, M.; Mitzi, D. B.; Gunawan, O.; Kellock, A. J.; Chey, S. J.; Deline, V. R. Antimony Assisted Low-Temperature Processing of $CuIn_{1-x}Ga_xSe_{2-y}S_y$ Solar Cells. *Thin Solid Films* **2010**, *519*, 852−856.

(20) Sutter-Fella, C. M.; Stückelberger, J. a.; Hagendorfer, H.; La Mattina, F.; Kranz, L.; Nishiwaki, S.; Uhl, A. R.; Romanyuk, Y. E.; Tiwari, A. N. Sodium Assisted Sintering of Chalcogenides and Its Application to Solution Processed $Cu_2ZnSn(S,Se)_4$ Thin Film Solar Cells. *Chem. Mater.* **2014**, *26*, 1420−1425.

(21) Gershon, B. T.; Lee, Y. S.; Mankad, R.; Gunawan, O.; Gokmen, T.; Bishop, D.; McCandless, B.; Guha, S. The Impact of Sodium on the Sub-Bandgap States in CZTSe and CZTS. *Appl. Phys. Lett.* **2015**, *106*, 123905.

(22) Liu, X.; Feng, Y.; Cui, H.; Liu, F.; Hao, X.; Conibeer, G.; Mitzi, D. B.; Green, M. The Current Status and Future Prospects of Kesterite Solar Cells: A Brief Review. *Prog. Photovoltaics* **2016**, *24*, 879−898.

(23) Ray, A.; Sathyanarayana, D. N. Infrared and Raman spectra of 2,4-dithiobiuret and its normal vibrations. *Spectrochim. Acta* **1975**, *31*, 899−904.

(24) Chrissafis, K.; Kyratsi, T.; Paraskevopoulos, K. M.; Kanatzidis, M. G. Crystal/Glass Phase Change in KSb_5S_8 Studied through Thermal Analysis Techniques. *Chem. Mater.* **2004**, *16*, 1932−1937.

(25) Kelley, C. K. Thermal Analysis Study of Antimony Sulphides. Report no.: WRDC-TR-89−2099 (WRDC/POSL, Wright-Patterson AFB, OH, 1989).

(26) Rodriguez-Carvajal, J. FULLPROF: A Program for Rietveld Refinement and Pattern Matching Analysis. *Abstracts of the Satellite Meeting on Powder Diffraction of the XV Congress of the IUCr*; 1990, p 127.

(27) Warren, B. E. *X-ray diffraction*; Dover publications: New York, NY, U.S.A., 1990.

(28) Grossberg, M.; Krustok, J.; Raudoja, J.; Raadik, T. The Role of Structural Properties on Deep Defect States in Cu_2ZnSnS_4 Studied by Photoluminescence Spectroscopy. *Appl. Phys. Lett.* **2012**, *101*, 102102.

(29) Scheer, R.; Schock, H. *Chalcogenide Photovoltaics*; Wiley-VCH: Weinheim, Germany, 2011.

(30) Gershon, T.; Lee, Y. S.; Antunez, P.; Mankad, R.; Singh, S.; Bishop, D.; Gunawan, O.; Hopstaken, M.; Haight, R. Photovoltaic Materials and Devices Based on the Alloyed Kesterite Absorber (Ag

DOI: 10.1021/acs.chemmater.6b01499
Chem. Mater. 2016, 28, 4991−4997

$_x$Cu$_{1-x}$)$_2$ ZnSnSe $_4$. *Adv. Energy Mater.* **2016**, DOI: 10.1002/aenm.201502468.

DOI: 10.1021/acs.chemmater.6b01499
Chem. Mater. 2016, 28, 4991−4997